

Radio Monitoring of the Tidal Disruption Event Swift J164449.3+573451. IV. Continued Fading and Non-Relativistic Expansion

Y. CENDES,¹ T. EFTEKHARI,¹ E. BERGER,¹ AND E. POLISENSKY²

¹*Center for Astrophysics | Harvard & Smithsonian, Cambridge, MA 02138, USA*

²*Remote Sensing Division, Naval Research Laboratory, Washington, DC 20375, USA*

ABSTRACT

We present continued radio and X-ray observations of the previously relativistic tidal disruption event (TDE) Swift J164449.3+573451 (Sw 1644+57) extending to about 9.4 years post disruption, as part of ongoing campaigns with the Jansky Very Large Array (VLA) and the *Chandra* X-ray observatory. We find that the X-ray emission has faded below detectable levels, with an upper limit of $\lesssim 3.5 \times 10^{-15}$ erg cm⁻² s⁻¹ in a 100 ks observation, while the radio emission continues to be detected and steadily fade. Both are consistent with forward shock emission from a non-relativistic outflow, although we find that the radio spectral energy distribution is better fit at these late times with an electron power law index of $p \approx 3$ (as opposed to $p \approx 2.5$ at earlier times). With the revised spectral index we find $\epsilon_B \approx 0.01$ using the radio and X-ray data, and a density of ≈ 0.04 cm³ at a radius of $R \approx 0.65$ pc ($R_{\text{sch}} \approx 2 \times 10^6 R_{\odot}$) from the black hole. The energy scale of the blastwave is $\approx 10^{52}$ erg. We also report detections of Sw 1644+57 at 3 GHz from the first two epochs of the VLA Sky Survey (VLASS), and find that $\sim 10^2$ off-axis Sw 1644+57-like events to $z \sim 0.5$ may be present in the VLASS data. Finally, we find that Sw 1644+57 itself will remain detectable for decades at radio frequencies, although observations at sub-GHz frequencies will become increasingly important to characterize its dynamical evolution.

Keywords: black hole physics

1. INTRODUCTION

A tidal disruption event (TDE) occurs when a star wanders sufficiently close to a supermassive black hole (SMBH) to be torn apart by tidal forces. In recent years, the number of observed TDEs has increased dramatically, primarily thanks to wide-field optical time-domain surveys¹. So far, only about 10 TDEs (about 10% of the known sample) have been detected in the radio band during dedicated follow-up observations (see Table 1; Alexander et al. 2020). In these cases, the radio emission points to non-relativistic outflows with an energy scale of $\sim 10^{37} - 10^{39}$ erg s⁻¹.

The TDE Sw 1644+57 remains unusual in this context. It was first detected as a γ -ray/X-ray event on 2011 March 28 by the *Swift* Burst Alert Telescope (BAT), although further analysis showed discernible emission as early as 2011 March 25 (Burrows et al. 2011). Multi-wavelength observations in the radio, millimeter, near-

IR, and optical were obtained shortly after discovery, and along with the high energy emission pointed to the launch of a relativistic jet (Bloom et al. 2011; Burrows et al. 2011; Zauderer et al. 2011; Berger et al. 2012). Subsequently, two additional potential relativistic TDEs have been discovered (Cenko et al. 2012; Brown et al. 2015), although Sw 1644+57 remains by far the best-studied case.

Continued monitoring of Sw 1644+57 revealed a sharp decline by about 2 orders of magnitude in its X-ray emission ≈ 500 days post disruption, corresponding to the relativistic jet shutting off (Zauderer et al. 2013). The subsequent X-ray emission has instead been shown to be an extension of the spectral energy distribution (SED) from the radio band, produced by the interaction of the blastwave with the ambient medium. The early radio/mm emission, and subsequent addition of X-ray information, have allowed us to track the velocity and energy scale of the blastwave, as well as the density profile of the circumnuclear medium (Berger et al. 2012; Zauderer et al. 2013; Eftekhari et al. 2018).

Here, we present continued X-ray and radio observations of Sw 1644+57 on a timescale of about 2390 to

Corresponding author: Yvette Cendes
yvette.cendes@cfa.harvard.edu

¹ See <http://tde.space>

3430 days post disruption. We use these most recent observations to continue tracking the blastwave energy and circumnuclear medium density profile. In Section 2, we present our new observations. In Section 3 we model the radio data, in conjunction with the X-ray data determine the location of the cooling frequency, and carry out an equipartition analysis to determine the physical properties of the outflow and ambient medium. In section 4 we discuss our findings in the context of the ongoing evolution of Sw 1644+57, and the implications of its detection in VLASS. We summarize our conclusions in Section 5.

2. OBSERVATIONS

Our previous work presented radio and mm observations of Sw 1644+57 extending to about 1895 d post disruption, and X-ray observations extending to about 2020 d post disruption (Zauderer et al. 2011; Berger et al. 2012; Zauderer et al. 2013; Eftekhari et al. 2018). Here we present continued radio and X-ray observations.

2.1. Radio Observations

We obtained radio observations of Sw 1644+57 with the Karl G. Jansky Very Large Array (VLA) spanning from L- to K-band (1 – 26.5 GHz; see Table 1; Program ID: 17B-198; PI: Eftekhari). All times are measured relative to 2011 March 25, corresponding to the time of first discernible γ -ray emission. We processed the data using the Common Astronomy Software Application package (CASA; McMullin et al. 2007) accessed through the python-based `pwkit` package² (Williams et al. 2017). We performed bandpass and flux density calibration using 3C286 for all observations and frequencies and J1638+5720 for the phase calibrator. We obtained all flux densities and uncertainties via the `imtool` program in `pwkit`.

In addition to our dedicated observations, we examined observations from the Very Large Array Sky Survey (VLASS; Lacy et al. 2020) at a frequency of 3 GHz (S-band) and report a detection of 1.2 ± 0.2 mJy in the “quick look” images from 2017 October 7 (Day 2388), and a detection of 0.3 ± 0.2 mJy on 2020 August 4 (Day 3434; see Table 1). Additionally, we identified data collected by the VLA Low-band Ionosphere and Transient Experiment (VLITE; Clarke et al. 2016) during our dedicated observation on 2018 January 18 (Day 2493) and report a 3σ upper limit at 350 MHz of $\lesssim 2.5$ mJy (Table 1).

2.2. X-Ray Observations

Table 1. VLA Radio Observations

Date (UTC)	δt (d)	Frequency (GHz)	Flux Density (mJy)
2017 Oct 7	2388*	3.0	1.2 ± 0.2
2018 Jan 20	2493	0.35	< 2.5
		1.5	1.04 ± 0.06
		2.6	1.39 ± 0.03
		3.4	1.29 ± 0.03
		6.0	0.84 ± 0.01
		9.8	0.53 ± 0.01
		14.7	0.34 ± 0.01
	21.8	0.22 ± 0.01	
2018 Nov 17	2795	1.5	< 0.3
		3.0	0.97 ± 0.03
		6.0	0.60 ± 0.01
		9.8	0.40 ± 0.02
		14.7	0.25 ± 0.01
		21.8	0.16 ± 0.03
2020 Aug 4	3434*	3.0	0.3 ± 0.2

NOTE—New VLA observations of Sw 1644+57, with upper limits quoted as 3σ .

* Flux density measurement from the VLA Sky Survey.

The *Chandra* X-ray observations were obtained on 2018 February 5 – 11 and August 6 (Day 2516: 47.2 ks; Day 2690: 50.9 ks; Program IDs: 19700497 and 19700757; PI: Eftekhari) using the Advanced CCD Imaging Spectrometer (ACIS-S). We analyzed the observations using standard ACIS data filtering, using CALDB within the CIAO software package (v4.12). For source detection, we performed a targeted extraction using an aperture size of $1.5''$ and an annular background region with inner and outer radii of $2''$ and $6''$, respectively, obtaining an individual net count rate and source significance for each observation.

Both of our observations yielded non-detections (see Table 2). We calculated the unabsorbed fluxes (0.3 – 10 keV) with PIMMS (v4.10), based on the assumption of forward shock emission where $\nu_X > \nu_c$ and $p = 3$ (see below), leading to a power law index of $\Gamma_X = 2.5$. Eftekhari et al. (2018) provided flux values for Days 1425 through 2019 assuming $p = 2.5$, and we therefore recalculate these fluxes with $\Gamma_X = 2.5$ for consistency. We assumed an absorbed power law model with an intrinsic absorption column $N_{\text{H,int}} = 2 \times 10^{22}$ cm⁻² (Mangano et al. 2016), and a Galactic absorption of $N_{\text{H,MW}} = 1.7 \times 10^{20}$ cm⁻² (Willingale et al. 2013).

² <https://github.com/pkgw/pwkit>

Table 2. *Chandra* X-ray Observations

Date (UTC)	δt (d)	Exposure Time (ks)	Net Counts	Net Count Rate (cts/s)	Flux (0.3 – 10 keV) (ergs/cm ² /s)
2015 Feb 20	1425	27.8	12.9 ± 3.6	(4.6 ± 1.3) × 10 ⁻⁴	(1.5 ± 0.4) × 10 ⁻¹⁴
2015 April 9	1473	18.7	3.9 ± 2.0	(2.1 ± 1.0) × 10 ⁻⁴	(7.3 ± 3.5) × 10 ⁻¹⁵
2015 Aug 25	1611	19.7	0	< 4.1 × 10 ⁻⁴	< 1.4 × 10 ⁻¹⁴
2016 Feb 1	1771	26.7	6.4 ± 2.4	(2.4 ± 1.0) × 10 ⁻⁴	(8.5 ± 4.0) × 10 ⁻¹⁵
2016 April 6	1836	24.6	5.8 ± 2.4	(2.3 ± 1.0) × 10 ⁻⁴	(8.4 ± 4.0) × 10 ⁻¹⁵
2016 19 June	1910	24.6	4.8 ± 2.1	(1.9 ± 0.9) × 10 ⁻⁴	(6.7 ± 3.2) × 10 ⁻¹⁵
2016 Oct 3	2019	24.6	2.6 ± 1.5	(1.1 ± 0.6) × 10 ⁻⁴	(3.9 ± 2.1) × 10 ⁻¹⁵
2018 Feb 5 – 11	2516	47.2	2.3 ± 2.7	< 1.3 × 10 ⁻⁴	< 5.3 × 10 ⁻¹⁵
2018 Aug 6	2690	50.9	2.0 ± 3.0	< 1.2 × 10 ⁻⁴	< 4.8 × 10 ⁻¹⁵

NOTE—Observed X-ray counts and source significance (1σ) for Sw 1644+57. Unabsorbed X-ray fluxes are calculated assuming an absorbed power law model with $\Gamma_X = 2.5$ (that is, assuming $p = 3$), $N_{\text{H,int}} = 2 \times 10^{22} \text{ cm}^{-2}$, and $N_{\text{H,MW}} = 1.7 \times 10^{20} \text{ cm}^{-2}$. Upper limits correspond to 3σ limits. Data for $\delta t = 1425, 1473$ are from [Levan et al. \(2016\)](#) (PI: Levan), and all other data before Day 2513 is from ([Eftekhari et al. 2018](#)), although the fluxes reported have been recalculated for the power law model described above.

3. MODELING AND ANALYSIS

3.1. Spectral Energy Distribution

As in our previous analyses of the radio emission from Sw 1644+57, we model the spectral energy distribution (SED) as self-absorbed synchrotron emission in order to determine the physical properties of the outflow and surrounding medium as a function of time. The SEDs at Days 2493 and 2795 are shown in Figure 1. The SEDs are defined by a peak flux density, $F_{\nu,p}$, at a peak frequency, ν_p , and by a power law slope related to the electron energy distribution, p . We previously found that at early times ν_p is defined by ν_m , the frequency associated with the minimum electron Lorentz factor of the electron distribution, γ_m , while at later times it is defined by the self-absorption frequency, ν_a ([Berger et al. 2012](#); [Zauderer et al. 2013](#); [Eftekhari et al. 2018](#)).

Following [Eftekhari et al. \(2018\)](#), we fit the SED with a weighted model that accounts for both possible versions of the peak frequency, using the models developed by [Granot & Sari \(2002\)](#) for synchrotron emission from GRB afterglows. When $\nu_a \ll \nu_m$ we have:

$$F_1 \equiv F_\nu(\nu_a) \left[\left(\frac{\nu}{\nu_a} \right)^{-s_1\beta_1} + \left(\frac{\nu}{\nu_a} \right)^{-s_1\beta_2} \right] \times \left[1 + \left(\frac{\nu}{\nu_m} \right)^{-s_2(\beta_2-\beta_3)} \right]^{-1/s_2}, \quad (1)$$

where β_n describes the spectral slopes above and below a break, and s_1 and s_2 are smoothing parameters that

describe the shape of the spectrum across each break. Here, $\beta_1 = 2$, $\beta_2 = 1/3$, and $\beta_3 = (1-p)/2$. When $\nu_m \ll \nu_a$, the spectrum is instead given by:

$$F_2 \equiv F_\nu(\nu_m) \left[\left(\frac{\nu}{\nu_m} \right)^2 e^{-s(\frac{\nu}{\nu_m})^{2/3}} + \left(\frac{\nu}{\nu_m} \right)^{5/2} \right] \times \left[1 + \left(\frac{\nu}{\nu_a} \right)^{-s_2(\beta_2-\beta_3)} \right]^{-1/s_2}, \quad (2)$$

where $\beta_2 = 5/2$ and $\beta_3 = (1-p)/2$. To obtain a smooth transition between the two regimes, we employ a weighted spectrum (Equation 3 in [Eftekhari et al. 2018](#)):

$$F = \frac{w_1 F_1 + w_2 F_2}{w_1 + w_2}, \quad (3)$$

where $w_1 = (\nu_m/\nu_a)^2$ and $w_2 = (\nu_a/\nu_m)^2$.

We determine the best fit using the Python Markov Chain Monte Carlo (MCMC) module `emcee` ([Foreman-Mackey et al. 2013](#)), assuming a Gaussian likelihood for the parameters F_ν , ν_a , and ν_m . We also included a parameter that accounted for systematic uncertainty for underestimates on the individual data points. Our priors were based on the assumption that all these parameters decrease over time, as seen in [Eftekhari et al. \(2018\)](#), and thus the value from the previous epoch was used as the upper limit for each respective parameter. The posterior distributions were sampled using 100 Markov chains, which were run for 2,000 steps, discarding the first 1,000 steps to ensure the samples have sufficiently converged.

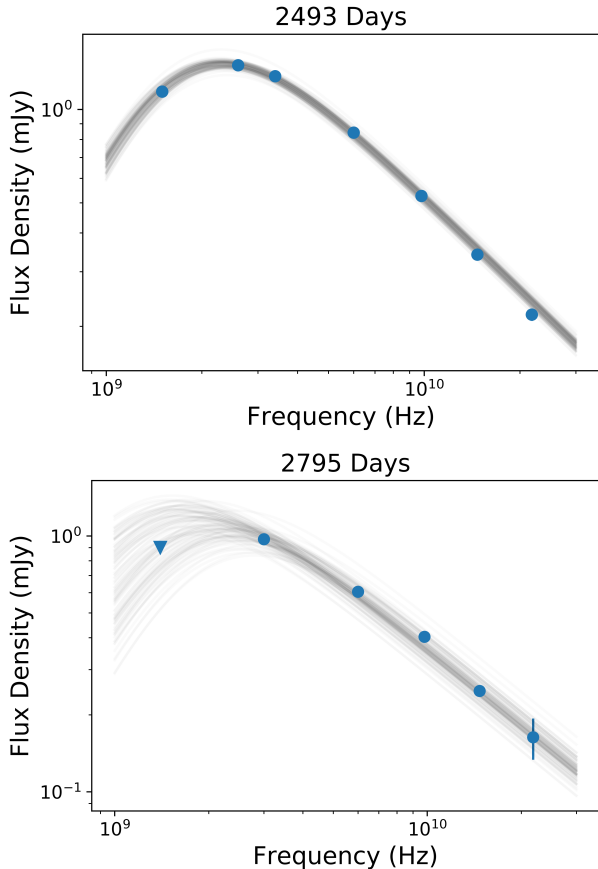


Figure 1. The radio spectral energy distributions at Days 2493 and 2795. The circles represent detections, and the triangle indicates a 3σ upper limit. The black lines are representative fits using MCMC with ν_a, ν_m , and F_ν as free parameters, and using a fixed value of $p = 3$.

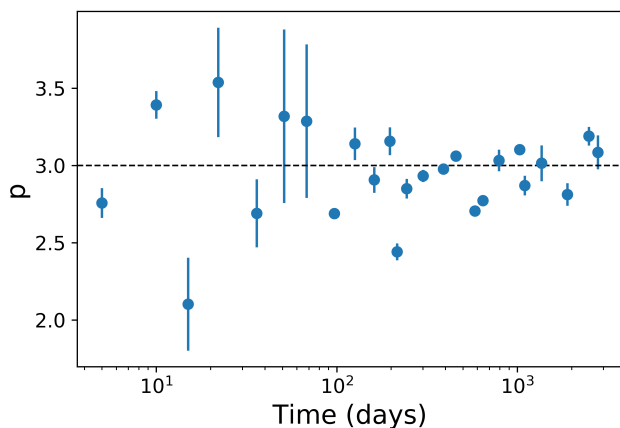


Figure 2. Best-fit values for the the electron power law index, p , as a function of time from our MCMC modeling of the individual radio/mm SEDs. The black dotted line marks the weighted mean value of $p \approx 3.0$ at $\gtrsim 100$ d, which is the value used in this work.

In Berger et al. (2012); Zauderer et al. (2013); Eftekhari et al. (2018), a value of $p = 2.5$ was adopted at earlier epochs, but here we fit for p as a free parameter. For this purpose we refit the entire radio data set and show the results for p in Figure 2. At early time ($\lesssim 100$ days) the value of p exhibits large variations and uncertainty. This is due to the high value of ν_p , and hence the paucity of data beyond the peak, as well as to interstellar scintillation, which leads to fluctuations in the observed flux density and hence the model fit (Berger et al. 2012). At later times we still find some scatter in p (primarily due to residual scintillation effects) but overall the weighted average after Day 100 is $p = 2.96 \pm 0.06$. We therefore adopt $p = 3$ in the remainder of our analysis, and refit all of the radio data beyond Day 700 with this value. We note that we explicitly checked the change in p by slicing the data to calculate the weighted average of p over time, but concluded the change in p is not a physical occurrence but instead due to more precise measurements at later times.

Following fitting with Equation 3, the resulting values for F_ν, ν_a , and ν_m are listed in Table 3 and plotted in Figure 3. We note explicitly that F_ν is the fitted flux density, which, due to the smoothing of the SED, is larger than the actual peak flux density, F_p , used in § 3.2. As in Eftekhari et al. (2018) we find an overall steady decline in ν_a and ν_m , with a corresponding decline in $F_{\nu,p}$. However, due to the difference in the adopted values of p we find systematic offsets of about a factor of 2.5 times higher for ν_a , a factor of 1.3 times higher for ν_m , and a factor of 7 times higher for $F_{\nu,p}$.

3.2. Equipartition Analysis

Using the inferred frequency and flux density parameters from the SED fitting in §3.1, we now infer the physical properties of the outflow using an equipartition analysis. In §3.3 we use the X-ray data to determine any deviation from equipartition, as found in our previous work (Eftekhari et al. 2018). In our analysis we follow the prescription of Barniol Duran et al. (2013). As already shown in Eftekhari et al. (2018), the outflow at late times is non-relativistic, leading to the following expressions for the equipartition radius and kinetic energy (see Equations 21 and 25 in Barniol Duran et al. 2013):

$$R_{\text{eq}} \approx (1.7 \times 10^{17} \text{ cm}) \times F_{p,\text{mJy}}^{8/17} d_{L,28}^{16/17} \nu_{p,10}^{-1} (1+z)^{-25/17} \\ \times f_A^{-7/17} f_V^{-1/17} (\nu_m/\nu_a)^{-1/34} 4^{1/17} \epsilon^{1/17} \quad (4)$$

Table 3. Spectral Energy Distribution Model Parameters

δt	$F_{\nu,p}$	$\log(\nu_a)$	$\log(\nu_m)$	$\log(\nu_c)$
[d]	[mJy]	[Hz]	[Hz]	[Hz]
791	$11.68^{+2.17}_{-1.30}$	$9.54^{+0.02}_{-0.02}$	$9.49^{+0.10}_{-0.11}$	$13.29^{+0.02}_{-0.02}$
1030	$9.82^{+2.67}_{-1.34}$	$9.37^{+0.04}_{-0.04}$	$9.31^{+0.12}_{-0.15}$	$13.44^{+0.04}_{-0.04}$
1100	$6.83^{+1.18}_{-0.99}$	$9.35^{+0.02}_{-0.02}$	$9.26^{+0.08}_{-0.08}$	$13.44^{+0.03}_{-0.03}$
1362	$3.35^{+1.49}_{-1.25}$	$9.32^{+0.03}_{-0.03}$	$9.18^{+0.15}_{-0.20}$	$13.42^{+0.05}_{-0.05}$
1894	$2.16^{+1.18}_{-0.86}$	$9.17^{+0.04}_{-0.03}$	$9.00^{+0.15}_{-0.25}$	$13.54^{+0.05}_{-0.05}$
2493	$0.84^{+0.42}_{-0.43}$	$9.16^{+0.04}_{-0.02}$	$8.91^{+0.15}_{-0.23}$	$13.51^{+0.06}_{-0.04}$
2795	$0.49^{+0.23}_{-0.22}$	$9.11^{+0.13}_{-0.08}$	$8.79^{+0.20}_{-0.23}$	$13.52^{+0.1}_{-0.15}$

NOTE—The model is described in §3 and in Granot & Sari (2002). We note that the values for ν_c are inferred from the equipartition calculation.

$$E_{\text{eq}} \approx (2.5 \times 10^{49} \text{ cm}) \times F_{p,\text{mJy}}^{20/17} d_{L,28}^{40/17} \nu_{p,10}^{-1} (1+z)^{-37/17} \\ \times f_A^{-9/17} f_V^{6/17} (\nu_m/\nu_a)^{-11/34} 4^{11/17} \\ \times [(11/17)\epsilon^{-6/17} + (6/17)\epsilon^{11/17}], \quad (5)$$

where $d_L = 1955$ Mpc is the luminosity distance, $z = 0.354$ is the redshift, and f_A and f_V are the area and volume filling factors, respectively, where we use $f_A = \theta_j^2$ with $\theta_j = 0.1$, and $f_V = \frac{4}{3}$ (Berger et al. 2012; Zauderer et al. 2013; Eftekhari et al. 2018). The factors of $4^{1/17}$ and $4^{11/17}$ for the radius and energy, respectively, arise from corrections to the isotropic number of radiating electrons ($N_{e,\text{iso}}$) in the non-relativistic case. Similarly, since at late times $\nu_m < \nu_a$, we include a correction factor of $(\nu_a/\nu_m)^{(p-2)/2}$ in $N_{e,\text{iso}}$, which leads to factors of $(\nu_a/\nu_m)^{(2-p)/34}$ in R_{eq} and $(\nu_a/\nu_m)^{11(2-p)/34}$ in E_{eq} . We further assume that the fraction of post-shock energy in relativistic electrons is $\epsilon_e = 0.1$, which leads to correction factors of $\xi^{1/17}$ and $\xi^{11/17}$ in R_{eq} and E_{eq} , respectively, where $\xi = 1 + \epsilon_e^{-1} \approx 11$. Finally, we parameterize a deviation from equipartition with a correction factor $\epsilon = (11/6)(\epsilon_B/\epsilon_e)$, where ϵ_B is the fraction of post-shock energy in magnetic fields.

The magnetic field and number of radiating electrons in the non-relativistic case are given by (see Equations 16 and 15 in Barniol Duran et al. 2013):

$$B \approx (1.3 \times 10^{-2} \text{ G}) \times F_{p,\text{mJy}}^{-2} d_{L,28}^{-4} (1+z)^7 f_A^2 R_{\text{eq},17}^4 \nu_{p,10}^5 \quad (6)$$

$$N_e \approx (1 \times 10^{54}) \times F_{p,\text{mJy}}^3 d_{L,28}^6 (1+z)^{-8} f_A^{-2} R_{\text{eq},17}^{-4} \nu_{p,10}^5 \\ \times (\nu_a/\nu_m)^{(p-2)/2}. \quad (7)$$

We calculate the number density of radiating electrons as $n_{\text{ext}} = 4N_e/V$, where $V = 4/3\pi R^3$ is the volume of the emission region.

The inferred outflow and external medium parameters as a function of time are plotted in Figure 4, using $\epsilon_B = 0.01$ (see §3.3); we include the values reported in Eftekhari et al. (2018) using $p = 2.5$ for reference. For the radius, we find values that are about a factor of 1.5 times smaller than in Eftekhari et al. (2018), but the trend of $R \propto t^{0.1}$, which has decreased when compared to the $R \propto t^{0.2}$ found by Eftekhari et al. (2018). For the energy, our values are about 5 times larger than in (Eftekhari et al. 2018), due to both the changes p and ϵ_B . We find a steady decline in the energy with $E \propto t^{-0.7}$. The magnetic field strength is about 6 times lower than in Eftekhari et al. (2018), and exhibits a steady decline with $B \propto t^{-0.5}$. Finally, we find values of $n_{e,\text{ext}}$ are lower than in Eftekhari et al. (2018) by a factor of 2, although within the error bars for that work, and declining with $n_{e,\text{ext}} \propto t^{-0.07}$.

3.3. Cooling Frequency and ϵ_B

Eftekhari et al. (2018) reported a deviation from equipartition in by searching for a cooling break using the optical/NIR and late-time ($\delta t \gtrsim 500$ d) X-ray data. They find $\epsilon_B \approx 10^{-3}$, two orders of magnitude lower than expected for equipartition (relative to the assumed value of $\epsilon_e = 0.1$). However, because here we use $p = 3$, thereby changing the steepness of the SED slope above ν_p , we expect that this will lead to a change in the location of the cooling frequency, ν_c , and hence ϵ_B . The cooling frequency is given by (Sari et al. 1998):

$$\nu_c = 2.8 \times 10^6 \gamma_c^2 \Gamma^2 B, \quad (8)$$

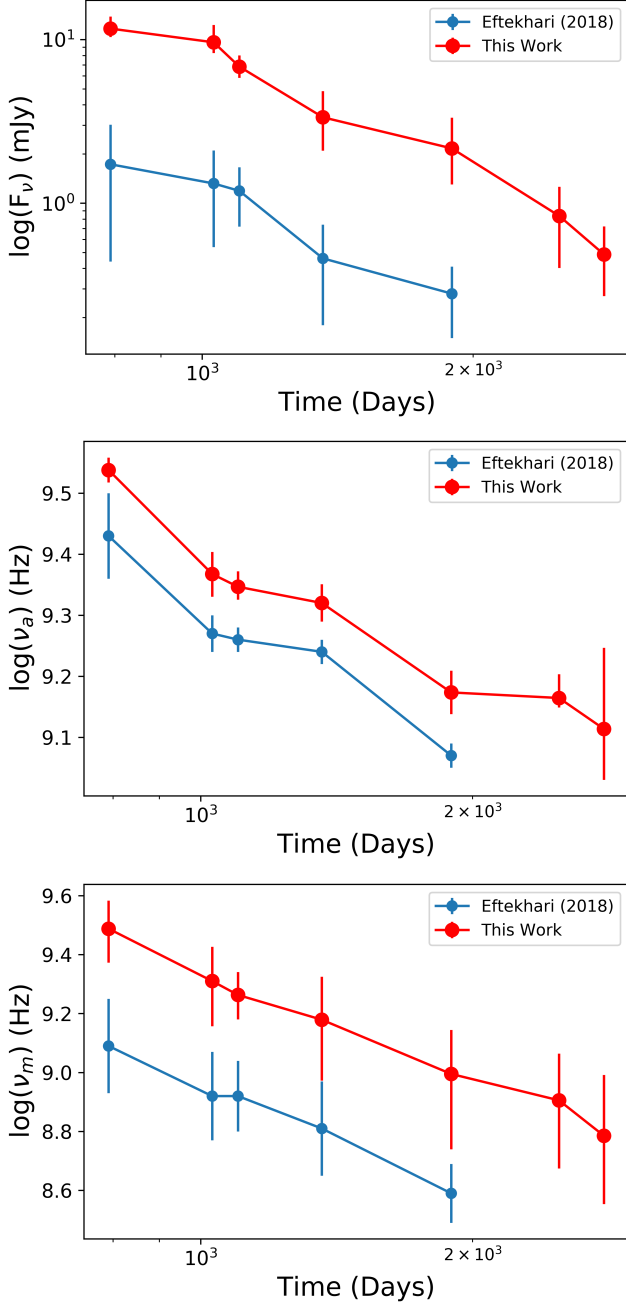


Figure 3. Time evolution of the parameters defining the radio SED from our epoch-by-epoch modeling here (red circles): $F_{\nu,p}$ (Top), ν_a (Middle), and ν_m (Bottom). We also show the results for the same parameters from [Eftekhari et al. \(2018\)](#), (blue). The two sets of values exhibit the same temporal trend, but differ in normalization due to the use of $p = 3$ in this work compared to $p = 2.5$ in [Eftekhari et al. \(2018\)](#).

where $\gamma_c = 5 \times 10^9 \epsilon_B^{-1} t_d^{-1} n_{\text{ext}}^{-1}$.

In Figure 5 we show the X-ray data at $\gtrsim 1400$ d along with an extrapolation of the radio models assuming equipartition ($\epsilon_B = 0.1$). We find that this model

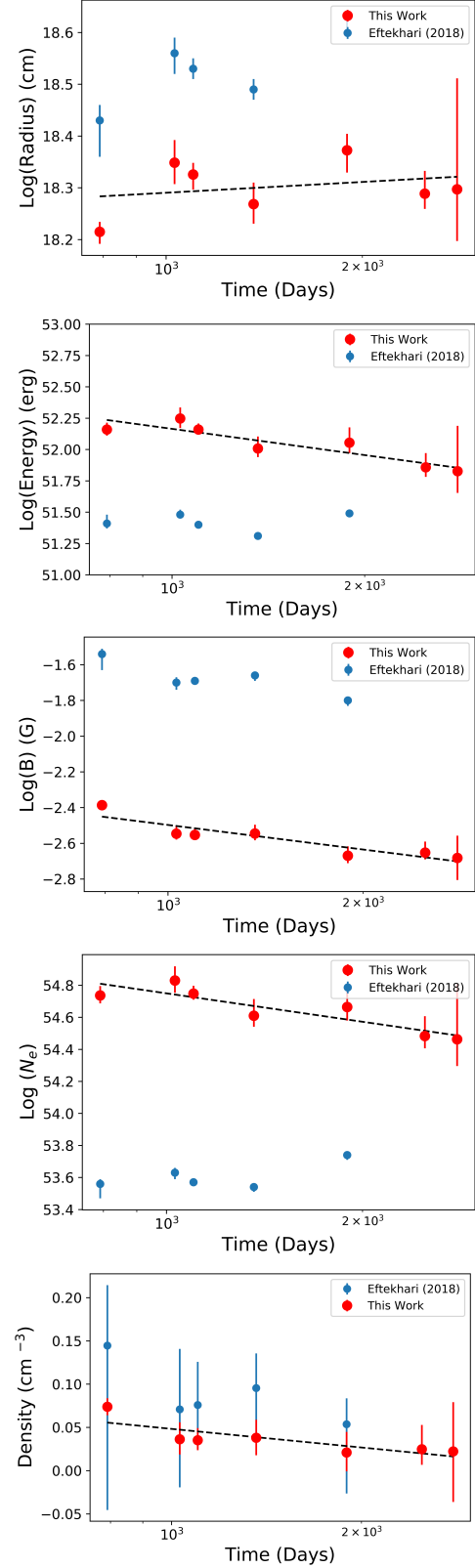


Figure 4. The radius, kinetic energy, magnetic field, number of radiating electrons, and ambient density from our equipartition analysis (red). We also show the results for the same parameters from [Eftekhari et al. \(2018\)](#), (blue). The two sets of values exhibit the same temporal trend, but differ in normalization due to the use of $p = 3$ in this work compared to $p = 2.5$ in [Eftekhari et al. \(2018\)](#).

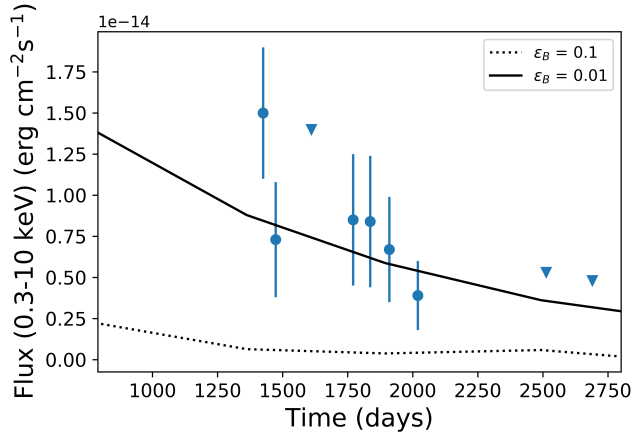


Figure 5. Late-time X-ray light curve, including the two upper limits measured here (blue). The lines are an extrapolation of the radio SEDs to the X-ray regime, assuming equipartition ($\epsilon_B = 0.1$; black dotted line) and a deviation from equipartition, with $\epsilon_B = 0.01$ (solid black line). The latter matches the X-ray observations.

underpredicts the observed X-ray flux. Instead, a model with $\epsilon_B \approx 0.01$ provides an adequate fit to both the amplitude and time evolution of the X-ray flux; see Figure 5. The blastwave and external medium parameters provided in the previous sections adopt this departure from equipartition.

4. DISCUSSION

Sw 1644+57 continues to be the best and longest studied relativistic TDE to date. Below we summarize the on-going evolution of the outflow and the ambient density profile, briefly discuss the implications of the VLASS detections, and cover what we can expect from observations of Sw 1644+57 in the future.

4.1. The Ongoing Evolution of Sw 1644+57

After Day ~ 700 the outflow from Sw 1644+57 transitioned to non-relativistic expansion (Eftekhari et al. 2018). Our most recent observations confirm this trend. The steady energy scale of the outflow on a timescale of $\sim 800 - 2800$ days (Figure 4) indicate no significant injection of energy from initially slow ejecta that may have caught up with the blastwave at late times. Similarly, the continued decline in X-ray emission (with the non-detections presented here) indicates that this band is still dominated by forward shock emission, and a jet has not been re-activated.

The continued radio observations extend our ability to measure the density profile around the supermassive black hole to a larger radius of about 0.7 pc. Using the time evolution of the blastwave radius and density of emitting particles, we find that the density

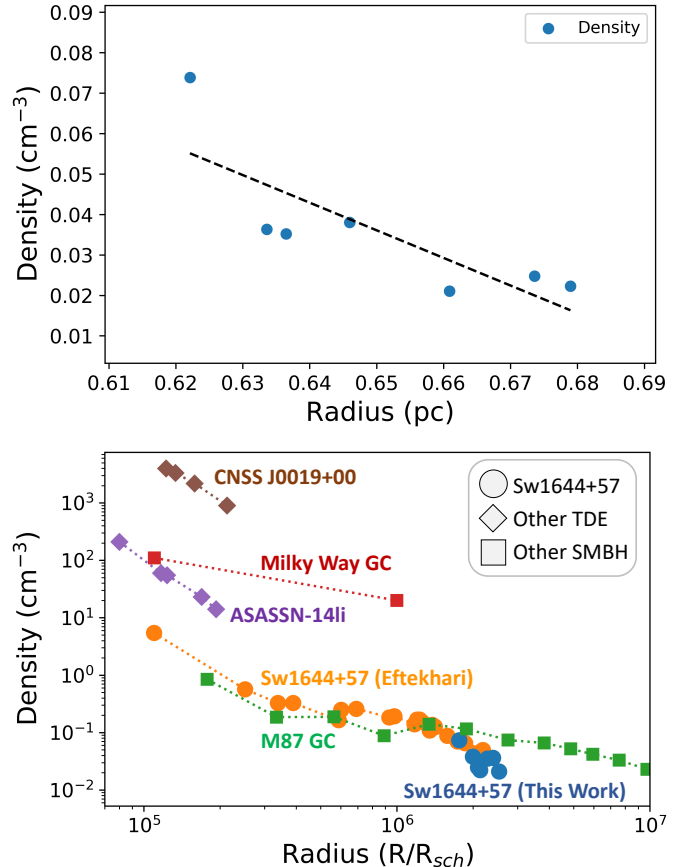


Figure 6. The circumnuclear density profile as a function of radius in parsecs (*Top*) and in units of R_{Sch} (*Bottom*; using $M_{\text{SMBH}} = 10^{6.5} M_{\odot}$). The data at smaller radii (from Eftekhari et al. 2018; yellow) are scaled by the difference in radius and density calculated in 3. For reference, we also include data for Sgr A* (red; Quataert 2004), M87 (green; Russell et al. 2015), and two TDEs with non-relativistic outflows (ASASSN-14li: Alexander et al. 2016, purple; CNSS J0019+00: Anderson et al. 2019, brown).

profile on a scale of $\approx 0.5 - 0.7$ pc roughly follows $n_{\text{ext}} \propto r^{-2}$; see Figure 6 (top). For the purpose of comparison with other supermassive black holes, we also scale the density profile to the Schwarzschild radius of the black hole (Figure 6; bottom). We find that the density in the environment of Sw 1644+57 is about 100 times lower than around Sgr A*, but comparable to that of M87. For reference, we also include two TDEs with non-relativistic outflows, ASASSN-14li (Alexander et al. 2016) and CNSS J0019+00 (Anderson et al. 2019), which overlap with the distances probed by Sw 1644+57 at early times. We find that both of those events occurred in higher density regions than Sw 1644+57.

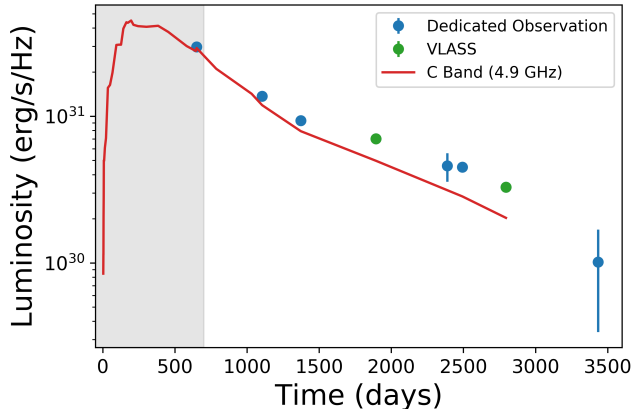


Figure 7. The radio spectral luminosity in S-band (~ 3 GHz; data points), and at C-band (4.9 GHz; red; Berger et al. 2012; Zauderer et al. 2013; Eftekhari et al. 2018). The shaded region indicates the time when the outflow is relativistic (Eftekhari et al. 2018).

4.2. VLASS Detection and Implications for Blind TDE Searches

The long-term radio emission from Sw 1644+57 raises the possibility of finding similar relativistic TDEs through their radio emission, even if the jet is initially oriented off-axis. Metzger et al. (2015) discussed the possibility of finding on-axis TDEs like Sw 1644+57 in the VLASS survey and find ~ 1 detectable event assuming a light curve duration of $\sim 10^3$ days and a typical off-axis peak luminosity about an order of magnitude lower than for Sw 1644+57. Recently, Anderson et al. (2019) reported the discovery of a radio transient (CNSS J001947.3+003527) in Stripe 82 survey data, which they interpret as an off-axis TDE. This event had a peak luminosity of 5×10^{28} erg s $^{-1}$ Hz $^{-1}$, about three orders of magnitude lower than Sw 1644+57.

Our two VLASS detections of Sw 1644+57, combined with our dedicated observations provide unique insight in the context of TDE blind radio detections. In Figure 7 we shows the light curve of Sw 1644+57 in S-band (3 GHz) and C-band (5 GHz). The spectral luminosity range traced by our observations so far is $\approx 3 \times 10^{31}$ erg s $^{-1}$ Hz $^{-1}$ at a peak time of ~ 0.55 yr to $\approx 10^{30}$ erg s $^{-1}$ Hz $^{-1}$ at about 9.5 yr. The outflow from Sw 1644+57 became non-relativistic on a timescale of ≈ 2 yr (Zauderer et al. 2013; Eftekhari et al. 2018), which can be used as a characteristic timescale for when similar events would become detectable even for an initial off-axis orientation; the spectral luminosity on this timescale was $\approx 2 \times 10^{31}$ erg s $^{-1}$ Hz $^{-1}$.

Given the slow cadence of a survey like VLASS (≈ 2.5 yr between successive epochs), it is most likely that similar events to Sw 1644+57 will be captured on a timescale

of \sim yr post-disruption. Thus, an event with a similar luminosity will be detectable at 10σ (≈ 2 mJy) to a redshift of $z \approx 0.6$ for an on-axis event. The radio emission from Sw 1644+57 post-peak evolves roughly as t^{-1} , so over the timescale of 2 VLASS epochs we expect that a similar source will fade by a factor of $\sim 2 - 3$ (depending on the phase of the light curve captured in the first epoch). At an initial detection of 10σ , this would be a measurable fading. Thus, we conclude that events like Sw 1644+57 can be captured in VLASS and shown to be fading to $z \sim 0.6$. Using the same approach for off-axis events, the lower luminosity means these events will be found in VLASS at $z \lesssim 0.5$.

Updating this distance with the calculation in Metzger et al. (2015), we find that there should be ~ 2 jetted TDE visible in VLASS. In the case of off-axis TDEs, the difference in rate would be $1.5\times$ lower due to the difference in comoving volumes between $z \sim 0.5$ and $z \sim 0.6$. Assuming a beaming factor of $\sim 10^2$, this yields $\sim 10^2$ off-axis TDE events in the VLASS survey. However, we emphasize that our estimate assumes the evolution of Sw 1644+57 is generic, and there may be a more significant difference between peak luminosity for on-axis and off-axis TDEs.

4.3. Future Observations

Sw 1644+57 is continuing to evolve as a non-relativistic outflow with an energy of $\approx 10^{52}$ erg into a ambient medium with a density of ≈ 0.1 cm $^{-3}$ on a scale of about 0.65 pc from the black hole (Figure 6). As we noted previously (e.g., Eftekhari et al. 2018), the radio emission will continue to be detectable with the VLA for decades. With a flux density of about 1 mJy at 3 GHz and a decline rate of about t^{-1} , the emission should be detectable for an order of magnitude longer in time (i.e., \sim century).

In terms of continued characterization of the outflow, it is essential to capture the peak of the SED, which is evolving to lower frequencies. In our latest multi-frequency observation at 7.7 yr post-disruption, we find that $\nu_p \approx 1.3$ GHz, which is at the lower frequency end of the VLA’s sensitive bands. We expect Sw 1644+57 to be detectable at $5\sigma \sim 1$ mJy at P-band (0.35 GHz) in a few hours of dedicated observing with the VLA or ~ 10 hr of commensal observing with VLITE. Another facility with sufficient sensitivity below 1 GHz is the Giant Meterwave Radio Telescope (GMRT), and we will report such follow-up observations in the future. At even lower frequencies, the Low-Frequency Array (LOFAR) is not sensitive enough to detect \sim mJy level emission, and the next generation VLA (ngVLA) proposal does not cover sub-GHz frequencies. We note that Sw 1644+57

is not visible from the future Square Kilometer Array (SKA) sites. As such, while the radio emission at GHz frequencies will continue to be detectable for decades, it is possible that a detailed characterization of the outflow may not be possible. Still, tracking the optically thin portion of the SED will allow us to determine changes in the dynamical evolution of Sw 1644+57, or evolution in the electron power law index, p .

Finally, the proposed Lynx X-ray Observatory may be able to detect emission from Sw 1644+57, depending on when (and if) it is launched, as well as whether Sw 1644+57 continues to evolve in X-rays at its present rate.

5. CONCLUSIONS

We presented new VLA radio data (1.5 – 22 GHz) and *Chandra* X-ray data extending to about 3400 days post-disruption, and used these observations to determine the continued dynamical evolution of the outflow and the density of the ambient medium. The combination of continued radio detections and X-ray upper limits allow us to characterize the synchrotron spectral energy distribution. We find that, unlike at early time, the electron power law at $\gtrsim 10^3$ days index is $p \approx 3$. The outflow continues to exhibit non-relativistic expansion, with a radius of about 2×10^{18} cm (0.65 pc) and a kinetic energy of about 10^{52} erg. The circumnuclear density is about 0.1 cm^{-3} .

We also report two detections of Sw 1644+57 in VLASS data, making it the first TDE detection in this sky survey (albeit not a blind detection). We estimate, based on the long-term evolution of Sw 1644+57, that

for events with similar luminosities and durations, ~ 2 on-axis and $\sim 10^2$ off-axis TDEs may be present in the VLASS data. We note, however, that Sw 1644+57 remains by far the most luminous TDE at radio frequencies so the detection rate in VLASS may be much lower. In addition, even if $\sim 10^2$ TDEs are present in the VLASS data, identifying these sources within the large survey footprint will not be trivial.

As Sw 1644+57 continues its slow fade, it will be detectable for decades with the VLA (and its successors), although the peak frequency continues to evolve to sub-GHz frequencies that are challenging to measure at the current brightness of Sw 1644+57. Still, continued observations of this unique event are essential to determine the long-term evolution of the outflow and the structure of the circumnuclear medium on sub-pc scales.

6. ACKNOWLEDGEMENTS

We thank Kate Alexander and Griffin Hosseinzadeh for conversations and input regarding the manuscript, and Wendy Lane for assistance with VLITE data. Support for this work was provided by the National Aeronautics and Space Administration through Chandra Award Numbers GO8-19087X and GO8-19098X issued by the Chandra X-ray Center, which is operated by the Smithsonian Astrophysical Observatory for and on behalf of the National Aeronautics Space Administration under contract NAS8-03060. The National Radio Astronomy Observatory is a facility of the National Science Foundation operated under cooperative agreement by Associated Universities, Inc. The scientific results reported in this article are based in part on observations made by the Chandra X-ray Observatory.

REFERENCES

- Alexander, K. D., Berger, E., Guillochon, J., Zauderer, B. A., & Williams, P. K. G. 2016, *ApJL*, 819, L25, doi: [10.3847/2041-8205/819/2/L25](https://doi.org/10.3847/2041-8205/819/2/L25)
- Alexander, K. D., van Velzen, S., Horesh, A., & Zauderer, B. A. 2020, arXiv e-prints, arXiv:2006.01159. <https://arxiv.org/abs/2006.01159>
- Anderson, M. M., Mooley, K. P., Hallinan, G., et al. 2019, arXiv e-prints, arXiv:1910.11912. <https://arxiv.org/abs/1910.11912>
- Barniol Duran, R., Nakar, E., & Piran, T. 2013, *ApJ*, 772, 78, doi: [10.1088/0004-637X/772/1/78](https://doi.org/10.1088/0004-637X/772/1/78)
- Berger, E., Zauderer, A., Pooley, G. G., et al. 2012, *ApJ*, 748, 36, doi: [10.1088/0004-637X/748/1/36](https://doi.org/10.1088/0004-637X/748/1/36)
- Bloom, J. S., Giannios, D., Metzger, B. D., et al. 2011, *Science*, 333, 203, doi: [10.1126/science.1207150](https://doi.org/10.1126/science.1207150)
- Brown, G. C., Levan, A. J., Stanway, E. R., et al. 2015, *MNRAS*, 452, 4297, doi: [10.1093/mnras/stv1520](https://doi.org/10.1093/mnras/stv1520)
- Burrows, D. N., Kennea, J. A., Ghisellini, G., et al. 2011, *Nature*, 476, 421, doi: [10.1038/nature10374](https://doi.org/10.1038/nature10374)
- Cenko, S. B., Krimm, H. A., Horesh, A., et al. 2012, *ApJ*, 753, 77, doi: [10.1088/0004-637X/753/1/77](https://doi.org/10.1088/0004-637X/753/1/77)
- Clarke, T. E., Kassim, N. E., Brisken, W., et al. 2016, in *Society of Photo-Optical Instrumentation Engineers (SPIE) Conference Series*, Vol. 9906, Proc. SPIE, 99065B, doi: [10.1117/12.2233036](https://doi.org/10.1117/12.2233036)
- Eftekhari, T., Berger, E., Zauderer, B. A., Margutti, R., & Alexander, K. D. 2018, *ApJ*, 854, 86, doi: [10.3847/1538-4357/aaa8e0](https://doi.org/10.3847/1538-4357/aaa8e0)
- Foreman-Mackey, D., Hogg, D. W., Lang, D., & Goodman, J. 2013, *PASP*, 125, 306, doi: [10.1086/670067](https://doi.org/10.1086/670067)

- Granot, J., & Sari, R. 2002, *ApJ*, 568, 820, doi: [10.1086/338966](https://doi.org/10.1086/338966)
- Lacy, M., Baum, S. A., Chandler, C. J., et al. 2020, *PASP*, 132, 035001, doi: [10.1088/1538-3873/ab63eb](https://doi.org/10.1088/1538-3873/ab63eb)
- Levan, A. J., Tanvir, N. R., Brown, G. C., et al. 2016, *ApJ*, 819, 51, doi: [10.3847/0004-637X/819/1/51](https://doi.org/10.3847/0004-637X/819/1/51)
- Mangano, V., Burrows, D. N., Sbarufatti, B., & Cannizzo, J. K. 2016, *ApJ*, 817, 103, doi: [10.3847/0004-637X/817/2/103](https://doi.org/10.3847/0004-637X/817/2/103)
- McMullin, J. P., Waters, B., Schiebel, D., Young, W., & Golap, K. 2007, in *Astronomical Society of the Pacific Conference Series*, Vol. 376, *Astronomical Data Analysis Software and Systems XVI*, ed. R. A. Shaw, F. Hill, & D. J. Bell, 127
- Metzger, B. D., Williams, P. K. G., & Berger, E. 2015, *ApJ*, 806, 224, doi: [10.1088/0004-637X/806/2/224](https://doi.org/10.1088/0004-637X/806/2/224)
- Quataert, E. 2004, *ApJ*, 613, 322, doi: [10.1086/422973](https://doi.org/10.1086/422973)
- Russell, H. R., Fabian, A. C., McNamara, B. R., & Broderick, A. E. 2015, *MNRAS*, 451, 588, doi: [10.1093/mnras/stv954](https://doi.org/10.1093/mnras/stv954)
- Sari, R., Piran, T., & Narayan, R. 1998, *ApJL*, 497, L17, doi: [10.1086/311269](https://doi.org/10.1086/311269)
- Williams, P. K. G., Gizis, J. E., & Berger, E. 2017, *ApJ*, 834, 117, doi: [10.3847/1538-4357/834/2/117](https://doi.org/10.3847/1538-4357/834/2/117)
- Willingale, R., Starling, R. L. C., Beardmore, A. P., Tanvir, N. R., & O'Brien, P. T. 2013, *MNRAS*, 431, 394, doi: [10.1093/mnras/stt175](https://doi.org/10.1093/mnras/stt175)
- Zauderer, B. A., Berger, E., Margutti, R., et al. 2013, *ApJ*, 767, 152, doi: [10.1088/0004-637X/767/2/152](https://doi.org/10.1088/0004-637X/767/2/152)
- Zauderer, B. A., Berger, E., Soderberg, A. M., et al. 2011, *Nature*, 476, 425, doi: [10.1038/nature10366](https://doi.org/10.1038/nature10366)